

Effect of high pressures on the formation of nitric oxide in lean, premixed flames

Philippe Versailles*

Combustion Mechanical Designer &
Technical Lead, ASME Member
Siemens Energy Canada Limited
Montréal, Québec H9P 1A5
Canada
philippe.versailles@siemens.com

Antoine Durocher

PhD Candidate, ASME Student Member
Department of Mechanical Engineering
McGill University
Montréal, Québec, H3A 0C3
Canada
antoine.durocher@mail.mcgill.ca

Gilles Bourque

Combustion Key Expert, ASME Fellow
Siemens Energy Canada Limited
Montréal, Québec H9P 1A5
Canada
gilles.bourque@siemens.com

Jeffrey M. Bergthorson

Associate Professor, ASME Fellow
Department of Mechanical Engineering
McGill University
Montréal, Québec, H3A 0C3
Canada
jeff.bergthorson@mcgill.ca

Adjunct Professor
Department of Mechanical Engineering
McGill University
Montréal, Québec, H3A 0C3
Canada
gilles.bourque@mcgill.ca

ABSTRACT

Increasingly stringent regulations are imposed on nitrogen oxides emissions due to their numerous negative impacts on human health and the environment. Accurate, experimentally validated thermochemical models are required for the development of the next generation of combustors. This paper presents a series of experiments performed in lean, premixed, laminar, jet-wall stagnation flames at pressures of 2, 4, 8, and 16 atm. To target post-flame temperatures relevant to gas turbine engines, the stoichiometry of the non-preheated methane-air mixture is adjusted to an equivalence ratio of 0.7. One-dimensional profiles of temperature and NO mole fraction are measured via laser-induced fluorescence (LIF) thermometry and NO-LIF, respectively, to complement previously published flame speed data [1]. The results reveal that, as the pressure increases, the maximum post-flame temperature stays relatively stable, and the concentration of NO produced through the flame front remains constant within uncertainty. Seven thermochemical models, selected for their widespread usage or recent date of publication, are validated against the experimental data. While all mechanisms accurately predict the post-flame temperature, thanks to consistent thermodynamic parameters, important disagreements are observed in the

*Corresponding author. Email: philippe.versailles@mail.mcgill.ca

NO concentration profiles, which highlights the need to carefully select the models used as design tools. The lack of pressure dependence of NO formation that many models fail to capture is numerically investigated via sensitivity and reaction path analyses applied to the solution of flame simulations. The termolecular reaction $\text{H} + \text{O}_2 (+\text{M}) \leftrightarrow \text{HO}_2 (+\text{M})$ is shown to hinder the production of atomic oxygen and hydrogen radicals at higher pressures, which inhibits the formation of nitric oxide through the N_2O pathway.

INTRODUCTION

Nitrogen oxides are involved in the formation of numerous pollutants, such as acid precipitations, ground-level ozone, smog, nutrient contamination of surface water, and fine aerosols that affect human health and the environment [2]. Governments imposed increasingly severe emission standards over the last decades, which induced major modifications to the architecture of combustors. For stationary applications, great improvements were achieved through a better control of the post-flame temperature field, namely by implementing lean premixed concepts, reducing mixture composition inhomogeneities through improved mixing, and decreasing cooling requirements to maximize the amount of air injected in the combustion chamber. These strategies allowed to minimize NO formation through the thermal (Zel'dovich) route, and achieve sub-10 ppm NO_x emissions [3], a level where the secondary N_2O , prompt, and NNH pathways are expected to significantly contribute [4]. An improved understanding of these chemical routes is, therefore, needed to inform the development of the next generation of low-emission combustors. Furthermore, accurate thermochemical models are required since numerical tools are intensively used to reduce development cost, and to design prototypes as close to production as possible. To properly constrain and validate the models, a comprehensive set of independent experimental data, collected in fundamental, laboratory burners minimizing combustor-specific effects [5], must be assembled [6, 7].

Several experimental studies, *e.g.*, [4, 8–11], investigated nitric oxide formation at low and ambient pressures for a variety of fuels, inert content, and stoichiometries. However, only a few experimental datasets, collected in McKenna [12–15], and counterflow [16] burners, were published at high pressures, and the ability of thermochemical models to accurately predict NO concentrations at these conditions remains unknown. In this paper, the experimental data measured by Versailles et al. [17] in laminar, lean, methane-air, jet-wall stagnation flames, and reported as absolute LIF signal intensities, are remastered using a direct calibration method to yield NO mole fractions. Originally limited to 8 atm, the dataset is extended to 16 atm, and supplemented with one-dimensional (1D) temperature profiles measured via multi-line NO-LIF thermometry along the axis of the burner. These measurements, along with the flame speed data provided in [1], form a complete ensemble of targets against which thermochemical models can be thoroughly validated at post-flame temperatures (≈ 1820 K) and pressures (up to 16 atm) relevant to gas turbine engines. In this paper, the dataset is employed to benchmark the predictions of seven thermochemical models available in the literature [18–25], and the most accurate, published by the National University of Ireland, Galway, is used to investigate the pressure dependence of NO formation in lean premixed flames.

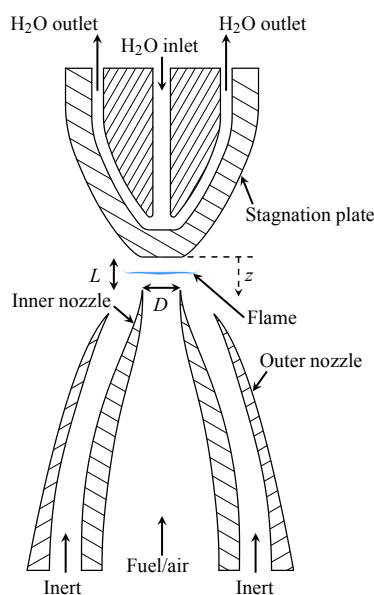


Fig. 1: Jet-wall stagnation burner [1]

EXPERIMENTAL METHOD

The present experiments were performed in the high-pressure, laminar flame facility at McGill University [1]. It consists of a jet-wall, stagnation flame burner installed in an optically accessible pressure vessel (0.29 m inner diameter, 0.86 m long) capable of continuous operation at the full-load pressure of modern aero-derivative gas turbines. The NO concentration and bulk flow temperature were measured via laser-induced fluorescence (LIF), and NO-LIF thermometry, respectively, adapted in the course of the work to high-pressure conditions.

Jet-wall, stagnation flame burner

The jet-wall, stagnation flame burner employed for the current experimental campaign is shown in Fig. 1. A well mixed stream of methane and air flows through the inner converging nozzle ($D = 10.2$ mm) and stagnates on a water-cooled plate located ≈ 9 mm downstream of the nozzle assembly. To prevent condensation and surface reactions [26], the plate is maintained at temperatures between 422 K and 489 K, approximately, throughout the experiments. To insulate the flame from the surroundings and improve its stability, it is shrouded by a stream of inert nitrogen gas [27]. In this configuration, the flame stabilizes at the location where its propagation speed matches the axial velocity of the incoming combustible mixture. As shown in Fig. 1, it is compact, lifted, stable, and readily accessible for laser-based diagnostics. For all conditions, the flame position is carefully adjusted to minimize interference from the burner boundaries. The chemical reactivity and production of pollutants are, therefore, sole functions of the properties of the reactant mixture.

During the experiments, the streams of nitrogen, air and methane are monitored using thermal mass flow controllers calibrated, for each operating pressure, using a dry-piston calibrator. This results in a relative uncertainty on the equivalence ratio of 0.71%. The temperatures of the reactants and stagnation plate are continuously measured using type-K thermocouples connected to a 24-bit isothermal data acquisition card. The pressure (P) is regulated by a digital controller connected to a pneumatic valve. The response

of the diaphragm-based, piezo-resistive sensor is calibrated against a NIST traceable gauge, yielding an uncertainty on P of 0.03 atm (3040 Pa). Further details on the burner, vessel, and equipment are found in [1].

NO laser-induced fluorescence

The concentration of nitric oxide is measured via two-dimensional, laser-induced fluorescence in the linear (weak irradiation) regime. A wavelength-tunable dye laser (Sirah Cobra-Stretch SL) filled with a solution of Coumarin 450 dye is pumped by the third harmonic of a Nd:YAG laser (Spectra-Physics Quanta-Ray Pro-230) to produce a beam at a wavelength of ≈ 452 nm. Its passage through a beta barium borate doubling crystal yields deep ultraviolet light at ≈ 226 nm. To obtain a fairly homogeneous energy profile, the beam travels through a homogenizer made of two plano-convex, cylindrical micro-lens arrays that create a number of smaller laser beams in the vertical direction, which are overlapped on the centreline axis of the burner by a plano-convex cylindrical lens to form an ≈ 9 mm tall, ≈ 1 mm wide, laser sheet [28].

Bessler et al. [29] studied many excitation and detection schemes, and concluded that A-X(0,0) excitation followed by red-shifted detection offers the highest NO laser-induced fluorescence signals, while minimizing interfering O₂-LIF. Consequently, the laser wavelength is adjusted to the spectral feature at ≈ 226.03 nm recommended by DiRosa et al. [30], which comprises the $S_{21}(4.5)$, $P_1(23.5)$, $P_{21} + Q_1(14.5)$, and $Q_2 + R_{12}(20.5)$ transitions of the A-X(0,0) electronic system of NO. The spontaneously emitted photons pass through a long-pass filter (Semrock LP02-224R), which blocks most of the Rayleigh scattering and transmits the A-X(0,1) and subsequent vibrational emission bands of nitric oxide, before being collected by an achromatic UV lens (Sodern Cerco 2178) mounted on extension rings for improved magnification. The photons are recorded by an intensified CCD camera (Dicam Pro, Gen II S-20 photocathode) exposed for 300 ns, with a 4 (vertical) by 8 (horizontal) pixel binning to increase the signal-to-noise ratio.

By invoking laser-induced fluorescence in the linear (weak irradiation) regime, the NO-LIF signal per unit laser energy for a given pixel on the ICCD detector, F_{NO} , can be written as [17]:

$$F_{\text{NO}} = \frac{S_{\text{NO}}}{E_L} = \frac{S_{\text{Raw}} - S_{\text{Bkg}_0}}{E_L} - F_{\text{Bkg}_1}, \quad (1)$$

where S_{NO} is the NO-LIF signal; E_L is the mean of the time-integrated laser pulse power profiles measured with a high-speed photodiode (Thorlabs DET10A) and an 1 GHz sampling rate oscilloscope (Picoscope 2207B); S_{Raw} is the raw signal measured by the camera (average of 5,000 images with laser irradiation); S_{Bkg_0} is a combination of laser-independent background signals, e.g., flame chemiluminescence, camera dark noise, surface reflections, etc. (measured by averaging 2,000 images of the flame without laser excitation); and F_{Bkg_1} is the signal per unit energy of laser-dependent interfering signals, such as O₂-LIF, CO₂-LIF, and scattering [29]. For each location along the axis of the burner, the F_{NO} values of 20 pixels (≈ 4.2 mm) in the vicinity of the centerline are averaged to yield an 1D profile of LIF signal intensity, which is then corrected for spatial variations in the laser sheet energy using the average of 2,000 LIF images measured in a cold, non-reacting stream of 300 ppm of NO in N₂.

To determine F_{Bkg_1} , the method of Versailles et al. [17], which does not assume that the background intensity is invariant to the laser wavelength as typically done [16, 31], is employed. As shown in Fig. 2 and detailed in [17], two excitation spectra without (orange curve) and with 53.7 ppm of nitric oxide seeded in the reactants (green curve) are measured at laser wavelengths ranging from 226.005 nm to 226.115 nm. One hundred twenty images are averaged at each wavelength, corrected for S_{Bkg_0} , and normalized by E_L . The subtraction of both spectra corresponds to the excitation spectrum of pure NO (blue curve). An iterative algorithm then determines the appropriate fraction (C_{Bkg}) of the NO spectrum (blue curve) to remove from the seeded trace to yield a background signal devoid of NO resonant features (black curve). The procedure is repeated for each axial location to obtain an one-dimensional profile of C_{Bkg} , which is smoothed by a least-squares adjusted sextic Bézier curve. To further reduce random oscillations in the axial noise profile, 5,000 images in seeded and unseeded flames are averaged at the on-resonance wavelength. For each axial position, the difference between both signals is multiplied by the local value of the sextic polynomial, and subtracted of the fluorescence intensity in the seeded flame, to yield the 1D profile of F_{Bkg_1} to be inserted in eq. (1).

Figure 2 illustrates the inherent difficulty to perform NO-LIF measurements at supra-atmospheric conditions; as P increases, the fluorescence signal of NO (blue curve) diminishes¹, while the intensity of the background interference rises. Namely, at 16 atm, the significantly broadened NO spectral features are barely recognizable in the unseeded spectrum. Under such conditions, the background signal determination procedure described above is ineffective. An alternate technique, inspired from [16, 31], is then implemented. *A priori*, on- and off-resonance wavelengths where the interfering signal is equal are unknown. However, taking advantage of the data collected at 8 atm and processed with the method of Versailles et al. [17], a range of wavelengths from 226.06 nm to 226.08 nm is identified over which the background trace is relatively constant, while the NO-LIF signal varies. The spectrum of the background signal is then obtained by iteratively determining the fraction of the NO-LIF signal (blue curve in Fig. 2 (d)) to remove from the seeded trace (green curve) to minimize the sum of squares of the difference between the background intensity at each of the wavelengths in the range 226.06 nm to 226.08 nm. Because of the wide variability in the C_{Bkg} values in the post-flame region, the adjustment of the sextic Bézier polynomial is unsuccessful. Consequently, the value of C_{Bkg} is calculated as the average of 10 pixels neighbouring a single position approximately halfway between the flame front and the stagnation surface, and used to determine F_{Bkg_1} as previously described.

Laser-induced fluorescence in the linear regime can be described by eq. (2), where X_{NO} is the mole fraction of NO molecules; $N(T, P)$ is the number density; f_{LIF} , generally provided by a LIF model, is the number of photons emitted per unit molecule of NO, and unit laser energy; $f_B(T)$ is the Boltzmann fraction of NO molecules in the state excited by the laser; λ is the laser wavelength; $\Delta\nu_L$ is the spectral width of the laser; $\Gamma(\Delta\nu_L, T, P, X_i)$ is the dimensionless overlap fraction; B_{12} is the Einstein constant of photon absorption; A_{21} is the rate constant of spontaneous emission; $Q_{21}(T, P, X_i)$ is the rate constant of non-radiative collisional quenching; and C_{opt} is the optical constant of the LIF system.

$$F_{NO} = X_{NO} \cdot N \cdot f_{LIF}(f_B, \lambda, \Delta\nu_L, \Gamma, B_{12}, A_{21}, Q_{21}) \cdot C_{opt} \quad (2)$$

¹For lean flames, the consumption of nitric oxide seeded into the reactants is negligible. Therefore, the blue spectra in Figs. 2 (a-d) correspond to a concentration of ≈ 53.7 ppm of NO, which does not vary with P .

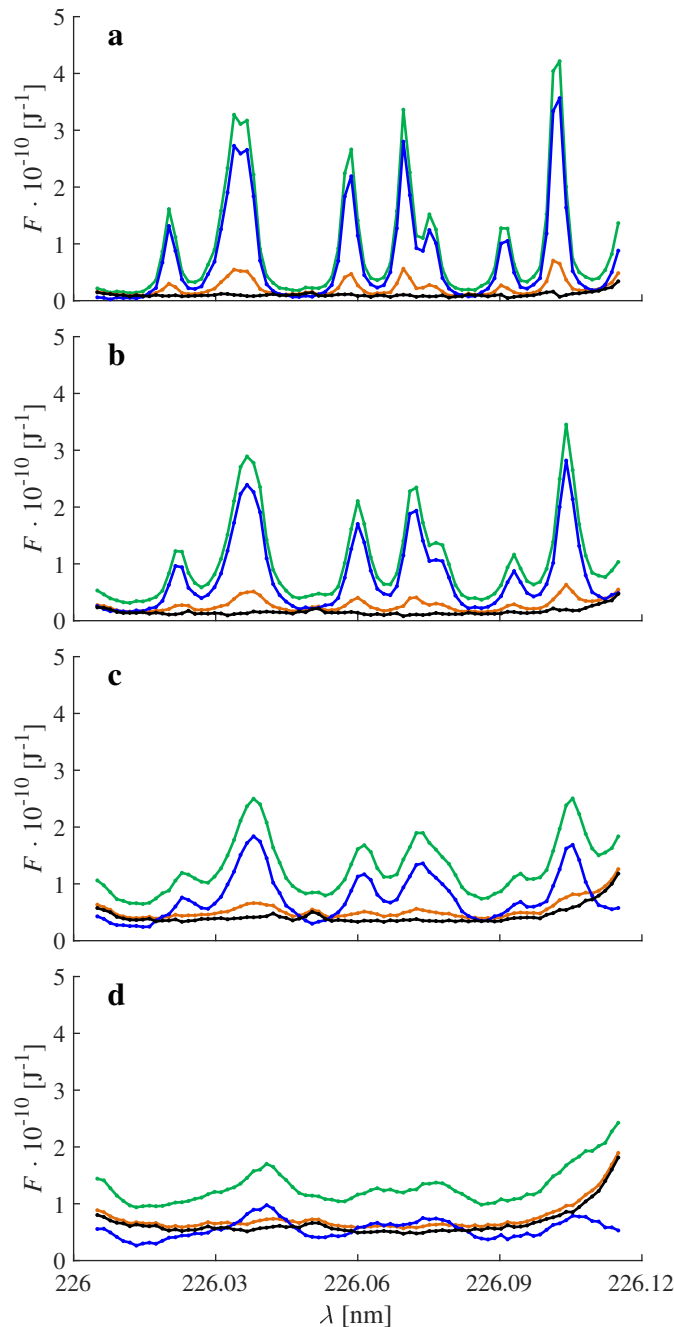


Fig. 2: Iterative background determination method applied in the post-flame region of the 2 atm (a), 4 atm (b), 8 atm (c), and 16 atm (d) flames. Legend: excitation spectra with (green) and without (orange) NO seeding, excitation spectra of pure NO (blue), and estimated background signal (black). On-resonance excitation is performed on the absorption band located at ≈ 226.04 nm

Some of these parameters can be calculated. However, species and temperature profiles must be hypothesized, which introduces uncertainty. Instead, a direct calibration procedure is used here. Five thousand LIF images collected in a flame seeded with 53.7 ppm of NO are averaged to yield $F_{NO,s}$ in eq.3. To remove the contribution of the nitric oxide produced by the flame, the LIF signal measured in the unseeded flame, F_{NO} , is deducted of $F_{NO,s}$. Assuming that the seeded NO molecules are inert through the

flame, a condition verified numerically and generally valid for lean flames [16], the net LIF signal can be written as:

$$F_{\text{NO},s} - F_{\text{NO}} = 53.7 \text{ ppm} \cdot N \cdot f_{\text{LIF}} \cdot C_{\text{opt}} \quad (3)$$

Given the relatively small amount of nitric oxide injected in the reactant stream, it is assumed that the bulk temperature and concentration of the main combustion products are identical in both, seeded and unseeded, flames. Hence, all parameters other than the NO mole fraction in the right-hand-side term of eqs. (2) and (3) are equal. It follows that the experimental mole fraction of NO molecules is calculated as:

$$X_{\text{NO}} [\text{ppm}] = \frac{F_{\text{NO}}}{F_{\text{NO},s} - F_{\text{NO}}} \cdot 53.7 \text{ ppm} \quad (4)$$

To develop eq. (4), it is hypothesized that C_{opt} is identical in eqs. (2) and (3). However, self-absorption (trapping) of the fluorescence signal by the surrounding nitric oxide molecules, which are at different concentrations in the seeded and unseeded flames, could invalidate this assumption. To assess the importance of this phenomenon, photon mean-free paths of 5.9 m (at 16 atm) to 15.5 m (at 2 atm) were calculated². These values are 2 to 3 orders of magnitude larger than the characteristic radius of the flame (approximately equal to D). Therefore, self-absorption of the NO-LIF signal is negligible. Also, it must be noted that absorption of the LIF signal by main combustion products, such as hot carbon dioxide and water vapour [29], if significant, does not affect the calibration since their concentration is the same in the seeded and unseeded flames.

NO-LIF thermometry

The temperature of the gas mixture is measured using a multi-line, one-dimensional, NO-LIF thermometry method [32, 33] using the equipment described in the previous section. The reactant stream is seeded with 537.4 ppm of NO, a concentration expected to have a minimal impact on the flame properties, namely the temperature of the products [33]. The wavelength of the laser is varied to cover multiple features of the NO excitation spectrum, whose respective intensity is temperature-dependent as shown in Fig. 3. For each axial position, a fitting procedure adjusts a series of parameters (the relative intensity of the spectrum (multiplier), the baseline (background) signal and its inclination, the laser line width (Gaussian and Lorentzian contributions), and the wavelength shift of the whole spectrum) to minimize the sum of squares of the difference between the measured and simulated excitation spectra, and extract the bulk gas temperature to an accuracy of $\approx 5\%$ at 2000 K [33].

Traditionally [9, 32, 33], the three-level laser-induced fluorescence model LIFSim [34] is employed to generate the theoretical excitation spectra required by the fitting procedure. However, in the course of the work, it was observed that some features of the

²The calculations were performed for the seeded (calibration) flames. At these conditions, the concentration of NO molecules is expected to be the highest and, therefore, self-absorption most critical.

experimental spectra did not exactly overlap the simulated traces. A detailed comparison of the spectral position of the different transitions in the A-X (0,0) system of NO revealed significant differences between the predictions of LIFSim and LIFBASE [35]. A different methodology is, therefore, implemented here to generate the theoretical traces. A database of excitation spectra, solely accounting for Doppler broadening, is assembled for a wide range of temperatures based on the predictions of LIFBASE. The same parameters listed above are adjusted by the fitting procedure, the only difference being that the width of the Lorentzian distribution, which now needs to be convolved with the spectra of the database since this step was previously performed by LIFSim, is the combination of the laser spectral profile and the pressure-dependent collisional broadening. Owing to the more accurate spectral positions in LIFBASE, a more than threefold reduction in the residuals of the least-squares method is observed for the 2 atm flame.

As shown in Fig. 2, the background interference becomes increasingly important in comparison to the NO fluorescence signal at higher pressures. If improperly quantified, the interfering signals can have a detrimental impact on the accuracy of the measurements [33]. Consequently, a second excitation spectrum in an unseeded flame is subtracted of the trace collected in the seeded flame. This removes the contribution of the interfering signals, and yields the excitation spectrum of pure NO (analogous to the blue curves in Fig. 2).

For all pressures, excitation scans (with and without NO seeding) with a resolution of 0.623 picometres are performed for wavelengths extending from 225.0736 nm to 225.1976 nm. Fifty images are averaged at each wavelength, corrected for $S_{Bk_{g0}}$, normalized by the laser energy (E_L) and, finally, processed into spectra. While this range of laser wavelengths offers a favourable sensitivity of the spectra to the gas temperature, it suffers from weak NO-LIF signal intensities at high pressures, namely in the colder region through and upstream of the flame. To obtain more reliable data in this zone, a second set of measurements averaging sixty-six fluorescence images collected at 150 wavelengths (2.0134 pm resolution) between 226.2145 nm and 226.5045 nm is performed for the 8 and 16 atm flames.

Quasi-one-dimensional flame modelling

Table 1: Experimentally determined boundary conditions. Absolute uncertainties are shown within parentheses.

P [atm]	ϕ	l [mm]	u_{inlet} [m/s]	$du/dz _{inlet}$ [1/s]	T_{inlet} [K]	T_{wall} [K]
2 (0.03)	0.7 (0.005)	8.17 (0.05)	0.2029 (0.0008)	48.33 (4.91)	291 (2)	422 (5)
4 (0.03)	0.7 (0.005)	8.12 (0.05)	0.1288 (0.0004)	28.43 (2.31)	293 (2)	445 (5)
8 (0.03)	0.7 (0.005)	6.62 (0.05)	0.0754 (0.0002)	15.10 (0.94)	292 (2)	440 (5)
16 (0.03)	0.7 (0.005)	5.15 (0.05)	0.0473 (0.0001)	10.56 (0.75)	293 (2)	489 (5)

The jet-wall burner was purposely designed to yield flat, axisymmetrical flames [36,37] producing 1D fields of species concentration, temperature, density, and axial velocity in the vicinity of the centreline axis. Coupled with an axisymmetrical stream function, they allow to reduce the three-dimensional continuity, Navier-Stokes, and energy and species conservation equations to

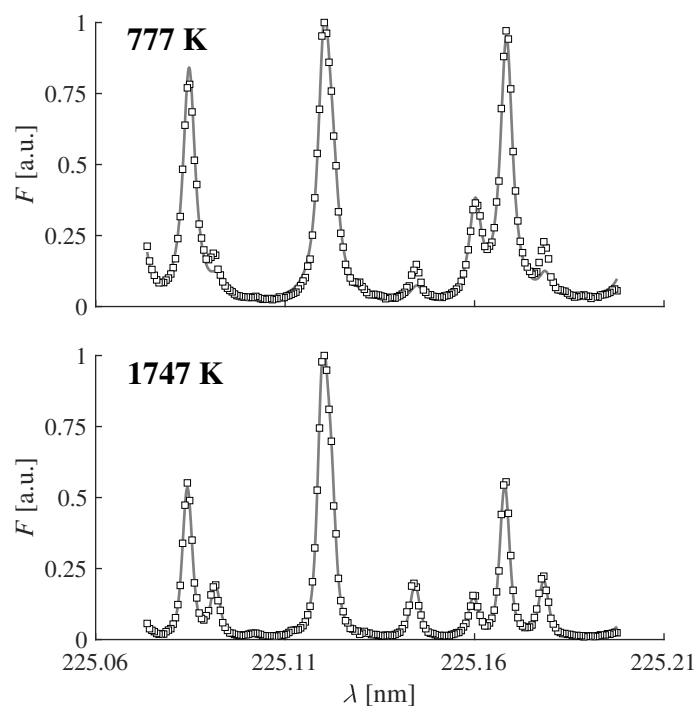


Fig. 3: Excitation spectra obtained within the front (top), and in the post-flame region (bottom) of the 2 atm flame. Legend: experimental data (square symbols), and numerical spectra least-squares adjusted to the experimental data (grey curves).

a quasi-1D formulation [38], implemented in Cantera 2.3 [39]. Radiative heat loss and the mixture-averaged formulation of the transport coefficients are included in the flame simulations, converged to absolute and relative tolerance levels of 10^{-9} and 10^{-5} , respectively, on highly resolved meshes achieving gradient and curvature parameters of 0.05 and 0.075, respectively. The boundary conditions (BC) for the flame simulations are reported in Table 1. The equivalence ratio is obtained from the mass flow rates of fuel and air provided by the thermal mass flow controllers, the temperatures collected using thermocouples, and the velocity BCs measured by Particle Tracking Velocimetry [1, 37].

The flame simulations are performed with seven thermochemical models selected for their wide usage in industry and academia, detailed modelling of the chemistry, date of release, or design philosophy: GRI-Mech 3.0 (GRI) [18]; the 2016 version of the San Diego mechanism (SD) with the nitrogen chemistry published in 2004³ [19]; the Combustion Science & Engineering, Inc. (CSE) model [20]; the high-temperature version of the mechanism from the National University of Ireland, Galway (NUIG) [21, 22]; the Konnov mechanism release 0.6 [23]; the high-temperature chemistry (version 1412) from the CRECK Modeling Group (CRECK) at Politecnico di Milano [24]; and the mechanism provided with the recently published review paper on the nitrogen chemistry of Glarborg et al. [25] (ARG).

³An updated version of the NO chemistry was released in 2018. However, it does not include all NO formation routes known to proceed in flames of gaseous hydrocarbon fuels. Namely, the prompt (Fenimore) pathway is excluded. For this reason, the more complete version 2004 is used here.

EXPERIMENTAL AND NUMERICAL RESULTS

The experimental temperature profiles along the axis of the burner are shown in Fig. 4 (symbols), where the water-cooled stagnation plate is located at $z = 0$ mm, and the outlet of the nozzle at $z \approx 9$ mm. As expected, the temperature is initially low, then rises rapidly through the front to reach a value close to the adiabatic flame temperature, and finally decreases in the thermal boundary layer (TBL) close to the plate due to convective heat loss. The temperature in the post-flame region outside of the TBL is observed to minimally change with the pressure. This indicates that dissociation is minimal at such low flame temperatures. Otherwise, increasing the pressure would shift the equilibrium to larger, more stable molecules as per the Le Chatelier's principle, and a rise in flame temperature would be observed. It is noted, principally at 4 and 16 atm, that the temperature of the reactants is significantly higher than the value measured by the thermocouples (see Table 1). In this region, the residuals of the least-squares fitting routine are much higher (about one order of magnitude) than in the post-flame region, which is expected to negatively impact the accuracy of the LIF thermometry.

The predictions of the seven thermochemical mechanisms are shown by the curves in Fig. 4. All models are consistent with each other and with the experimental data in the post-flame region, which indicates that the models include an accurate, consistent set of thermodynamic coefficients. The slight reduction in the predicted temperature upstream of the TBL, which is caused by radiative heat loss, is not observed in the experimental data. This discrepancy is, however, within the bounds of uncertainty. Also, the temperature reduction in the thermal boundary layer is well captured by all models. The principal differences between the models and against the experimental data are observed in the flame front region. The spread in flame position is due to inconsistent predictions of flame reactivity [1]. Namely, in stagnation flows, an overestimation of the flame speed will result in a front located upstream of the experimental flame, and vice-versa.

The experimental profiles of NO mole fraction are shown in Fig. 5. As expected, nitric oxide is rapidly formed through the front mostly via the N_2O pathway, and then relatively slowly in the post-flame region, principally via the thermal route [17]. In the thermal boundary layer, X_{NO} decreases indicating that a fraction of the nitric oxide molecules formed through the flame are consumed. As explained above, the measurements at 16 atm are plagued by a significant amount of noise, such that only a single data point could be extracted. However, the general shape of the mole fraction profile should be similar to lower pressures as suggested by the simulations. As concluded in [17] based on the nominal concentrations at 2, 4 and 8 atm, the amount of NO formed through the flame front (numerical values indicated on the plots) slightly decreases monotonically with the pressure. However, considering the width of the error bars, as well as the new data at 16 atm, a more appropriate conclusion would be that NO formation in lean, premixed flames, dominated by the N_2O pathway, does not present a significant dependence to the pressure. This has important implications for engines. Namely, the current dataset collected at pressures and post-flame temperatures relevant to gas turbine combustors indicates that single-digit NO emissions are achievable from low to high loads, if the pre-mixer is carefully designed to provide very low unmixedness.

The NO concentration predictions of the seven thermochemical models are shown by the curves in Fig. 5. A wide variability is observed for all investigated pressures. Furthermore, many models provide X_{NO} values that significantly differ from the experimen-

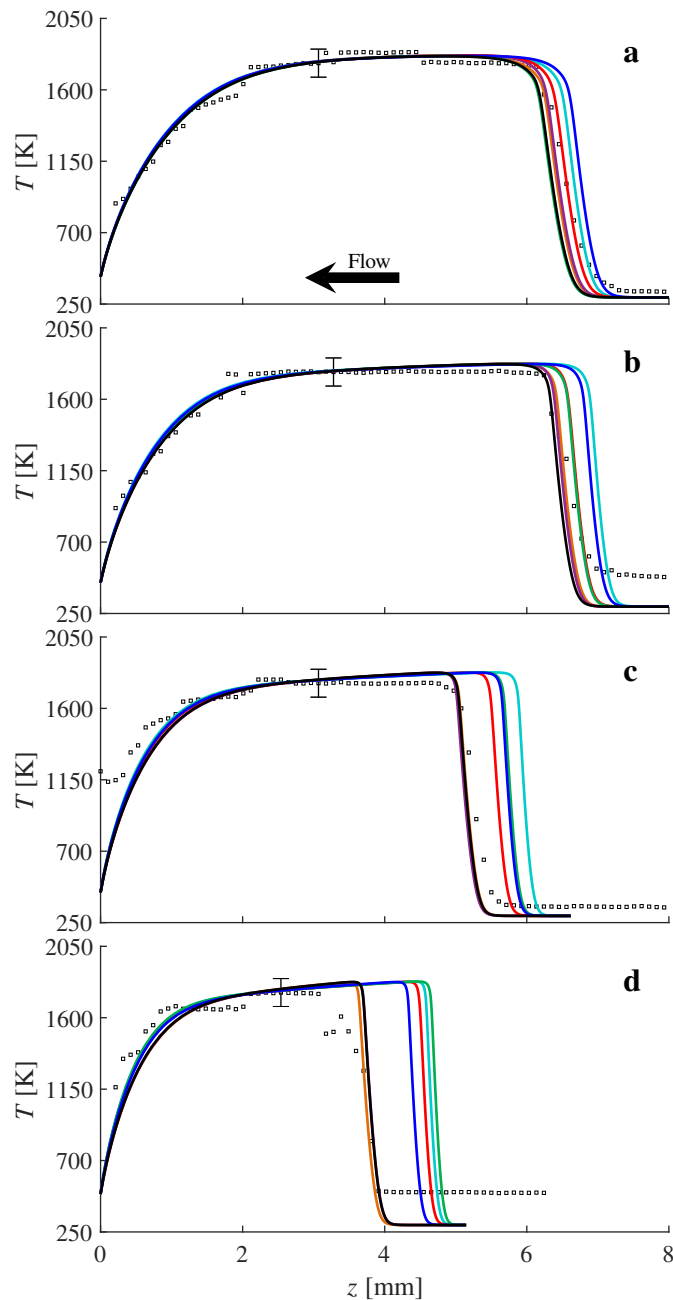


Fig. 4: One-dimensional profiles of temperature at 2 atm (a), 4 atm (b), 8 atm (c), and 16 atm (d). The plate is located at $z = 0$ mm, and the outlet of the nozzle at $z \approx 9$ mm. Legend: experiments (symbols), NUIG (orange), CRECK (purple), CSE (cyan), KON (green), SD (blue), GRI (red), and ARG (black).

tal data, *i.e.*, beyond the uncertainty bounds, which demonstrates the relevancy of the current dataset as optimization and validation targets for model development. Given the consistent temperature predictions presented in Fig. 4, it follows that these discrepancies are not caused by thermal effects, but rather by an incorrect modelling of the chemistry. In particular, the GRI model, which is widely used in industry and academia, under-predicts the experimental data for all conditions (as much as 50% at 8 atm). This implies that a concept, developed using the GRI mechanism to achieve a given emission level, could well miss the target once built. Also, many models do not accurately capture the pressure dependence of the NO mole fraction. Namely, the CSE, SD, and KON

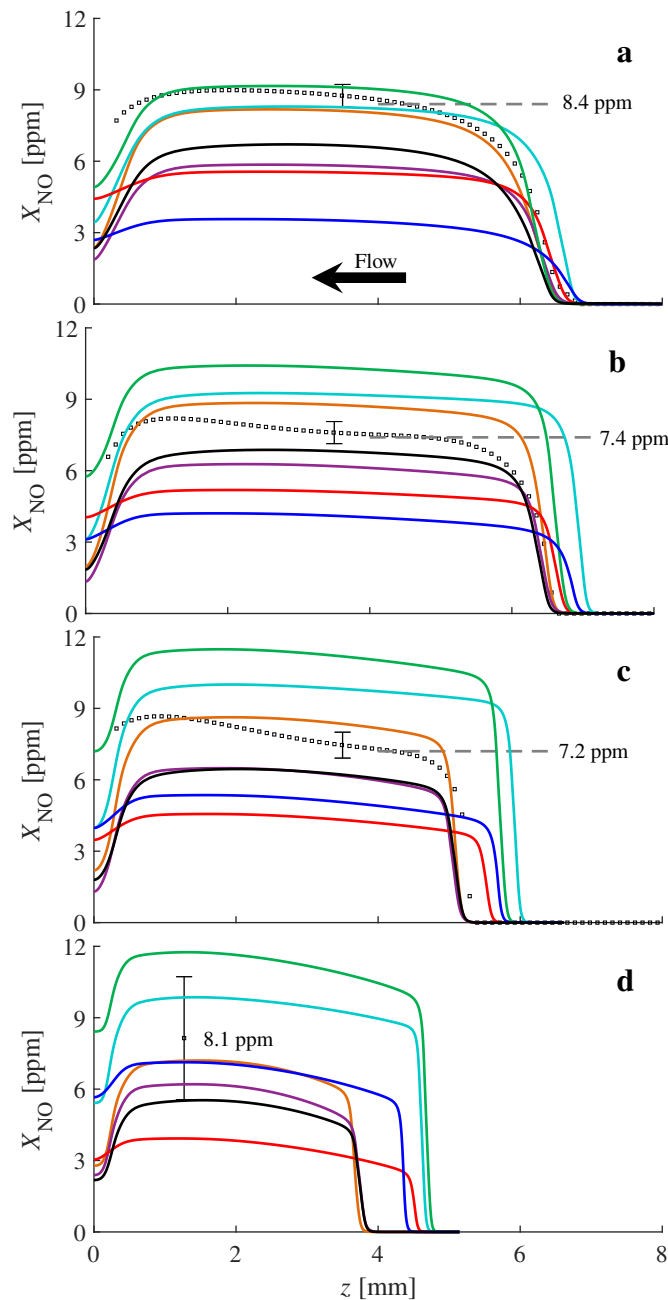


Fig. 5: One-dimensional profiles of NO mole fraction at 2 atm (a), 4 atm (b), 8 atm (c), and 16 atm (d). Same legend as Fig. 4. The error bars account for the accuracy of the LIF method, as well as the effect of the uncertainty of the BCs estimated with flame simulations performed with the NUIG model.

mechanisms predict a continuous increase in X_{NO} with the pressure, and these variations are significant in view of the experimental uncertainty. Namely, the values provided by the KON mechanism are within the bounds of error at 2 atm, but completely outside at 16 atm, while the opposite is observed for the SD model. Finally, although they sometimes provide numerical values outside of the experimental bounds of uncertainty, the most recently published CRECK, ARG and NUIG models generally present the best performance in terms of pressure dependence and NO mole fraction, as well as flame speed and location as demonstrated in [1]. These observations highlight the importance of properly selecting the chemical models used in the design of low-emission engines.

termolecular reaction:



The other, prompt (Fenimore), NNH, and thermal, routes play a minor role through the front of the current lean, low-temperature flames. Once formed, the N_2O molecules are either transformed back into N_2 by the reverse of reaction (5) and by reaction (6); transformed into NO via reactions (7) and (8); or simply escape the control volume (grey-dashed arrow in the RPA diagram).

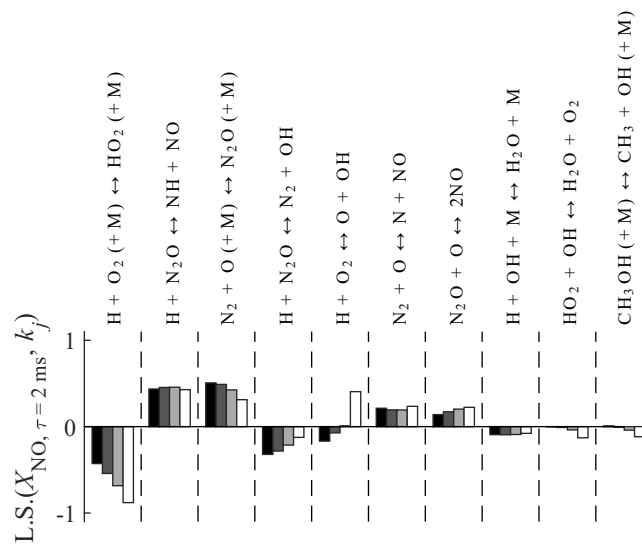


Fig. 7: Logarithmic sensitivity of the nitric oxide mole fraction at an axial position 2 ms downstream of the flame front. The bands are coloured based on a black (2 atm) to white (16 atm) colormap.

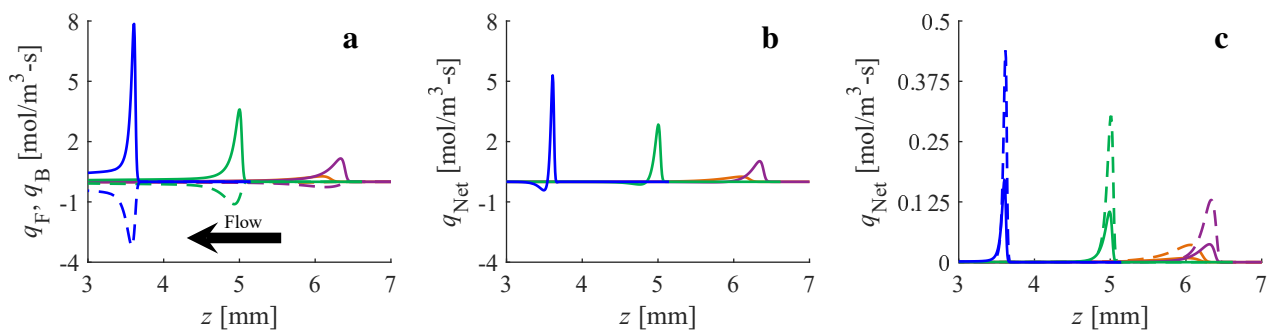


Fig. 8: Profiles of forward (solid curves, plot a), backward (dashed curves, plot a), and net (b) reaction rates of the reaction $\text{N}_2 + \text{O} (+\text{M}) \leftrightarrow \text{N}_2\text{O} (+\text{M})$, and net reaction rates of reactions $\text{N}_2\text{O} + \text{H} \leftrightarrow \text{NO} + \text{NH}$ (dashed curves, plot c) and $\text{N}_2\text{O} + \text{O} \leftrightarrow \text{NO} + \text{NO}$ (solid curves, plot c). Legend: $P = 2$ atm (orange), $P = 4$ atm (purple), $P = 8$ atm (green), and $P = 16$ atm (blue).

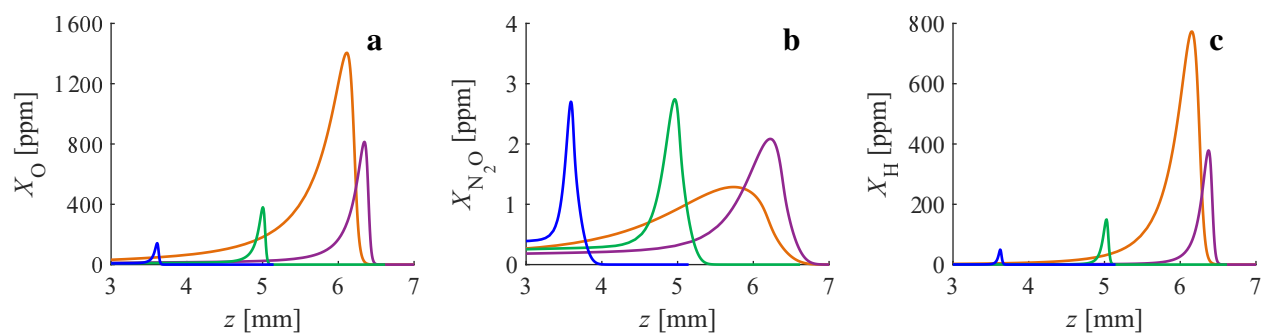


Fig. 9: Mole fraction profiles of atomic oxygen (a), N_2O (b) and atomic hydrogen (c). Same legend as Fig. 8.

The forward rate of reaction (5) can be written as:

$$\begin{aligned}
 q_F &= [\text{N}_2] \cdot [\text{O}] \cdot [\text{M}] \cdot k_F \\
 &\approx X_{\text{N}_2} \cdot X_{\text{O}} \cdot \left(\frac{P}{RT}\right)^3 \cdot k_F,
 \end{aligned} \tag{9}$$

where P is the pressure, R the universal gas constant, T the temperature, and k_F the specific rate of the forward reaction. Based on the cubic term in eq. (9), the pressure could be expected to significantly raise q_F and, consequently, the mole fractions of N_2O and NO . However, as shown in Fig. 5, P has a very weak influence on the formation of NO , even though the pressure is multiplied by a factor of 8 in the current experiments.

Figure 8 (a) presents the forward rate of reaction (5). It is noted that the maximum value of q_F increases with the pressure, however, not cubically; the maximum rate rises by a factor of ≈ 29 , while it would be expected to be multiplied by 512 (8^3) based on eq. (9) (in fact, more than 512 when considering the pressure dependence of k_F). Furthermore, the backward reaction accelerates rapidly as N_2O molecules are created, such that significant values of q_{Net} are limited to a thin layer within the flame front region (Fig. 8 (b)). Reaction (6), which proceeds preferentially in the forward direction, was observed to consume N_2O molecules at a much slower rate than the reverse of reaction (5). Furthermore, as shown in Fig. 8 (c), the net rates of reactions (7) and (8) are

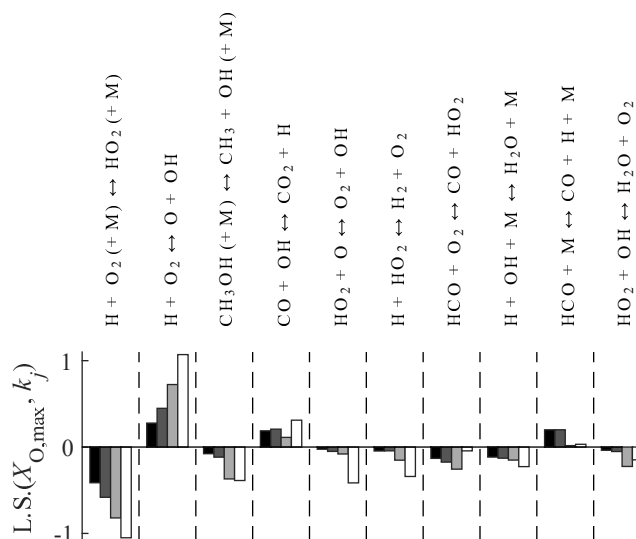


Fig. 10: Logarithmic sensitivity of the maximum atomic oxygen mole fraction to the specific rate of the individual reactions. Same legend as Fig. 7

negligible in comparison to the backward rate of reaction (5) (Fig. 8 (a)). It follows that the mole fraction profiles of N_2O , shown in Figure 9 (b), are primarily determined by the net rate of reaction (5). Namely, for all pressures, X_{N_2O} rises rapidly through the front, reaches a maximum value that moderately varies with the pressure, and then decays in the post flame region.

The mole fraction of N_2 is mainly dictated by the composition of the reactants, and does not change significantly with the pressure. Therefore, referring to eq. (9), the lower than expected rise in the forward rate of reaction (5) is related to the mole fraction of atomic oxygen. As shown in Fig. 9 (a), X_O , namely its maximum value achieved in the flame front region, decreases significantly with the pressure. To identify the main reactions causing this reduction, the logarithmic sensitivity of the peak value of X_O to the specific rate of the reactions was calculated at each pressure (see Fig. 10). As for nitric oxide, only a very small subset of the chemistry model has a significant influence on the concentration of atomic oxygen. Specifically, the termolecular reaction (10), presenting large negative values of L.S. that become larger on an absolute basis at higher pressures, is the most dominant. This reaction is well-known for its chain terminating effect leading to the second explosion limit in hydrogen-oxygen mixtures [42]. Through reaction path analyses tracking hydrogen atoms, this reaction was observed to favour the formation of water molecules in the current flames. Therefore, based on the simulated data, it is concluded that reaction (10), by depleting the pool of atomic oxygen radicals, restricts the forward rate of reaction (5) and inhibits the formation of N_2O molecules.



The net rates of reactions (7) and (8), which primarily evolve in the forward direction, are presented in Figure 8 (c). Interestingly, significant values of q_{Net} for these reactions are only observed within the flame front region, where the radicals required for

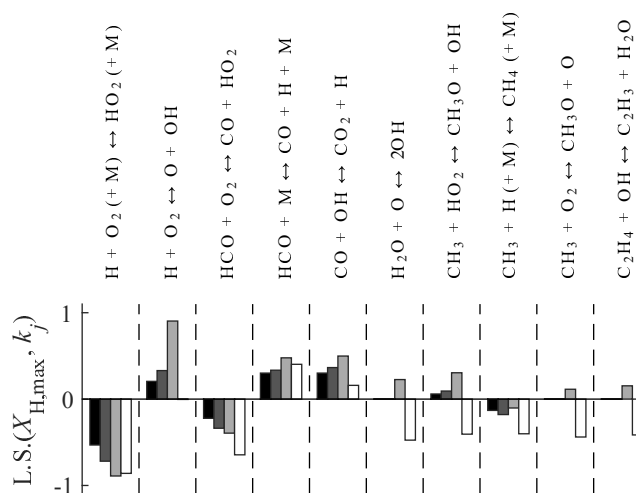


Fig. 11: Logarithmic sensitivity of the maximum atomic hydrogen mole fraction to the specific rate of the individual reactions. Same legend as Fig. 7.

their progress are available. That is, analogous to the prompt (Fenimore) route, the N_2O pathway is a rapid mechanism of NO formation that proceeds within the front. Similarly to eq. (9), applying the law of mass action suggests that the rate of these reactions should increase by a factor of 64 between 2 and 16 atm, if the mole fractions of O, H and N_2O , were to remain constant. However, the maximum value of q_{Net} only rises by factors of ≈ 20 and ≈ 12 for reactions (7) and (8), respectively. As discussed above, the termolecular reaction (10) has the strongest negative impact on the formation of oxygen atoms. Hence, its influence is not limited to the formation of N_2O molecules, it also inhibits their transformation into nitric oxide via reaction (7). Figure 11 shows the logarithmic sensitivity of the maximum value of X_H to the specific rate of the reactions. Again, the termolecular reaction (10), which consumes the hydrogen radical, is the most dominant. By hampering the formation of atomic hydrogen (see Fig. 9 (c)), it reduces the rate of reaction (8), and inhibits the formation of NO at higher pressures.

CONCLUSION

This paper presented one-dimensional profiles of nitric oxide mole fraction and temperature measured using laser-induced fluorescence, and multi-line, NO-LIF thermometry, respectively. The experiments were performed in a jet-wall, stagnation burner at pressures of 2, 4, 8, and 16 atm. The non-preheated methane-air mixture was adjusted to an equivalence ratio of 0.7 to achieve post-flame temperatures of ≈ 1820 K. For these conditions, nitric oxide is rapidly formed through the front via the N_2O pathway, and then relatively slowly in the post-flame zone by the thermal (Zel'dovich) route. While NO formation could be expected to be significantly favoured at high pressures due to the termolecular nature of the initiation reaction $N_2 + O(+M) \leftrightarrow N_2O(+M)$, the experimental data instead reveal that, within the bounds of uncertainty, the pressure has a very weak impact on the NO mole fraction, which remains below 10 ppm. This demonstrates that single digit NO emissions are achievable in dry low emission combustors, if the post-flame temperature field is properly managed to hinder the thermal (Zel'dovich) route.

The experimental data was used to validate the predictions of seven thermochemical models. While significant differences

in the flame reactivity caused discrepancies in the flame front position, all models provide post-flame temperatures consistent with the experimental data. On the other hand, a significant variability is observed among the numerical values of NO mole fraction provided by the models, and against the experiments. Namely, the GRI-Mech 3.0 mechanism, widely used in academia and industry, is shown to consistently under-predict the experimental data. Furthermore, many thermochemical models present an incorrect pressure dependence of NO mole fraction. This highlights the need to properly select the models employed for the design of combustion systems.

A detailed study of the nitrogen chemistry, applying sensitivity and reaction path analyses to the flame solutions obtained with the model of the National University of Ireland, Galway, was performed. The weak pressure dependence of nitric oxide formation through the N₂O pathway is strongly coupled to the termolecular reaction $H + O_2 (+M) \leftrightarrow HO_2 (+M)$, which gains in importance at higher pressures. This reaction, by depleting the pool of radicals, namely atomic oxygen and hydrogen, hampers the formation of N₂O molecules, and inhibits their transformation into nitric oxide. This conclusion, based on simulations, should be supported by future measurements of O, H and N₂O concentrations.

PERMISSION FOR USE

The content of this paper is copyrighted by Siemens Energy Canada Ltd. and is licensed to ASME for publication and distribution only. Any inquiries regarding permission to use the content of this paper, in whole or in part, for any purpose must be addressed to Siemens Energy Canada Ltd. directly.

Acknowledgements

The authors gratefully acknowledge the support of BioFuelNet Canada, the Natural Sciences and Engineering Research Council of Canada (NSERC), the Fonds de recherche du Québec - Nature et technologies (FRQNT), and Siemens Energy Canada Ltd.

Nomenclature

Thermochemical models

ARG	Argonne National Laboratory & Technical University of Denmark	[25]
CRECK	Politecnico di Milano	[24]
CSE	Combustion Science & Engineering, Inc.	[20]
GRI	GRI-Mech 3.0	[18]
KON	Lund University	[23]
NUIG	National University of Ireland, Galway	[21,22]
SD	University of California, San Diego	[19]

Symbols

A_{21}	rate constant of spontaneous emission	s^{-1}
B_{12}	Einstein constant of photon absorption	$m^2 J^{-1} s^{-1}$
BC	boundary condition	
C_{Bkg}	background coefficient	
C_{opt}	optical constant of the LIF system	m^{-3}
D	throat diameter of the inner nozzle	m
E_L	mean of the time-integrated laser pulse power profiles	J
f_B	Boltzmann fraction of molecules in the state excited by the laser	
f_{LIF}	number of photons emitted per unit molecule and laser energy	J^{-1}
F_{Bkg_1}	laser-dependent interfering signal per unit laser energy	J^{-1}
F_{NO}	NO-LIF signal per unit laser energy	J^{-1}
k_F	specific rate in the forward direction	mol, m^3, s
k_j	specific rate of reaction j	mol, m^3, s
l	length of the computational domain	m
L	nozzle-to-plate separation distance	m
L.S.	logarithmic sensitivity	
N	number density	m^{-3}
P	pressure	atm
q_B	backward reaction rate	$mol/m^3 \cdot s$
q_F	forward reaction rate	$mol/m^3 \cdot s$
q_{Net}	net reaction rate	$mol/m^3 \cdot s$
Q_{21}	rate constant of non-radiative collisional quenching	s^{-1}
R	universal gas constant	$m^3 \cdot atm/mol \cdot K$
S_{Bkg_0}	raw, laser-independent background signal	
S_{NO}	raw NO-LIF signal	
S_{Raw}	raw signal measured by the camera	
T	temperature	K
TBL	thermal boundary layer	
u	axial velocity	m/s
X_i	mole fraction of species i	
Y_i	mass fraction of species i	
z	axial position	m
Γ	dimensionless overlap fraction	
$\Delta\nu_L$	spectral width of the laser	cm^{-1}
λ	laser wavelength	nm
ρ	density	kg/m^3
τ	residence time downstream of the flame front	s
ϕ	equivalence ratio	

Subscripts

inlet at the inlet of the computational domain

s in the seeded flame

wall at the stagnation surface

References

- [1] Versailles, P., Durocher, A., Bourque, G., and Bergthorson, J. M., 2018. "Measurements of the reactivity of premixed, stagnation, methane-air flames at gas turbine relevant pressures". *ASME. J. Eng. Gas Turbines Power*, **141**(1), pp. 011027–1011027–10.
- [2] Vallero, D., 2014. *Fundamentals of Air Pollution*, 5th ed. Academic Press.
- [3] Lieuwen, T. C., Chang, M., and Amato, A., 2013. "Stationary gas turbine combustion: Technology needs and policy considerations". *Combust. Flame*, **160**(8), pp. 1311–1314.
- [4] Lipardi, A. C. A., Versailles, P., Watson, G. M. G., Bourque, G., and Bergthorson, J. M., 2017. "Experimental and numerical study on NO_x formation in CH₄-air mixtures diluted with exhaust gas components". *Combust. Flame*, **179**, pp. 325–337.
- [5] Bergthorson, J. M., and Thomson, M. J., 2015. "A review of the combustion and emissions properties of advanced transportation biofuels and their impact on existing and future engines". *Renew. Sust. Energy Rev.*, **42**, pp. 1393–1417.
- [6] Frenklach, M., Wang, H., and Rabinowitz, M. J., 1992. "Optimization and analysis of large chemical kinetic mechanisms using the solution mapping method - combustion of methane". *Prog. Energy Combust. Sci.*, **18**, pp. 47–73.
- [7] Frenklach, M., 2007. "Transforming data into knowledge - Process Informatics for combustion chemistry". *Proc. Combust. Inst.*, **31**(1), pp. 125–140.
- [8] Watson, G. M. G., Versailles, P., and Bergthorson, J. M., 2017. "NO formation in rich premixed flames of C₁-C₄ alkanes and alcohols". *Proc. Combust. Inst.*, **36**, pp. 627–635.
- [9] Watson, G. M. G., Versailles, P., and Bergthorson, J. M., 2016. "NO formation in premixed flames of C₁-C₃ alkanes and alcohols". *Combust. Flame*, **169**, pp. 242–260.
- [10] Bohon, M. D., Guiberti, T., and Roberts, W. L., 2018. "PLIF measurements of non-thermal NO concentrations in alcohol and alkane premixed flames". *Combust. Flame*, **194**, pp. 363–375.
- [11] Sutton, J., Williams, B., and Fleming, J., 2012. "Investigation of NCN and prompt-NO formation in low-pressure C₁-C₄ alkane flames". *Combust. Flame*, **159**(2), pp. 562–576.
- [12] Thomsen, D. D., Kuligowski, F. F., and Laurendeau, N. M., 1999. "Modeling of NO formation in premixed, high-pressure methane flames". *Combust. Flame*, **119**(3), pp. 307–318.
- [13] Reisel, J. R., and Laurendeau, N. M., 1994. "Laser-Induced Fluorescence measurements and modeling of nitric oxide formation in high-pressure flames". *Combust. Sci. Tech.*, **98**(1-3), pp. 137–160.
- [14] Reisel, J. R., and Laurendeau, N. M., 1995. "Quantitative LIF measurements and modeling of nitric oxide in high-pressure

C₂H₄/O₂/N₂ flames”. *Combust. Flame*, **101**, pp. 141–152.

- [15] Drake, M. C., Ratcliffe, J. W., Blint, R. J., Carter, C. D., and Laurendeau, N. M., 1991. “Measurements and modeling of flamefront NO formation and superequilibrium radical concentrations in laminar high-pressure premixed flames”. *Proc. Combust. Inst.*, **23**(1), pp. 387–395.
- [16] Pillier, L., Idir, M., Molet, J., Matynia, A., and De Persis, S., 2015. “Experimental study and modelling of NO_x formation in high pressure counter-flow premixed CH₄/air flames”. *Fuel*, **150**, pp. 394–407.
- [17] Versailles, P., Durocher, A., Bourque, G., and Bergthorson, J. M., 2018. “Nitric oxide formation in lean, methane-air stagnation flames at supra-atmospheric pressures”. *Proc. Combust. Inst.*, **37**(1), pp. 711–718.
- [18] Smith, G. P., Golden, D. M., Frenklach, M., Moriarty, N. W., Eiteneer, B., Goldenberg, M., Bowman, C. T., Hanson, R. K., Song, S., Gardiner, W. C., Lissianski, V. V., and Qin, Z., 1999. GRI-Mech 3.0. http://www.me.berkeley.edu/gri_mech/.
- [19] University of California at San Diego, 2016. “Chemical-Kinetic Mechanisms for Combustion Applications”, San Diego Mechanism web page, Mechanical and Aerospace Engineering (Combustion Research). <http://combustion.ucsd.edu>.
- [20] Gokulakrishnan, P., Fuller, C. C., Klassen, M. S., Joklik, R. G., Kochar, Y. N., Vaden, S. N., Lieuwen, T. C., and Seitzman, J. M., 2014. “Experiments and modeling of propane combustion with vitiation”. *Combust. Flame*, **161**(8), pp. 2038–2053.
- [21] Zhou, C. W., Li, Y., O’Connor, E., Somers, K. P., Thion, S., Keesee, C., Mathieu, O., Petersen, E. L., DeVerter, T. A., Oehlschlaeger, M. A., Kukkadapu, G., Sung, C. J., Alrefae, M., Khaled, F., Farooq, A., Dirrenberger, P., Glaude, P. A., Battin-Leclerc, F., Santner, J., Ju, Y., Held, T., Haas, F. M., Dryer, F. L., and Curran, H. J., 2016. “A comprehensive experimental and modeling study of isobutene oxidation”. *Combust. Flame*, **167**, pp. 353–379.
- [22] Zhang, Y., Mathieu, O., Petersen, E. L., Bourque, G., and Curran, H. J., 2017. “Assessing the predictions of a NO_x kinetic mechanism on recent hydrogen and syngas experimental data”. *Combust. Flame*, **182**, pp. 122–141.
- [23] Konnov, A. A., 2009. “Implementation of the NCN pathway of prompt-NO formation in the detailed reaction mechanism”. *Combust. Flame*, **156**(11), pp. 2093–2105.
- [24] CRECK Modeling Group, 2014. CRECK kinetics model (version 1412). <http://creckmodeling.chem.polimi.it/menu-kinetics/menu-kinetics-detailed-mechanisms>.
- [25] Glarborg, P., Miller, J. A., Ruscic, B., and Klippenstein, S. J., 2018. “Modeling nitrogen chemistry in combustion”. *Prog. Energy Combust. Sci.*, **67**, pp. 31–68.
- [26] Egolfopoulos, F. N., Zhang, H., and Zhang, Z., 1997. “Wall effects on the propagation and extinction of steady, strained, laminar premixed flames”. *Combust. Flame*, **109**(1-2), pp. 237–252.
- [27] Bergthorson, J. M., 2005. “Experiments and modeling of impinging jets and premixed hydrocarbon flames”. PhD thesis, California Institute of Technology.
- [28] Zimmermann, M., Lindlein, N., Voelkel, R., and Weible, K. J., 2007. “Microlens laser beam homogenizer: from theory to application”. *Proc. SPIE*, **6663**, pp. 666302–1–666302–12.
- [29] Bessler, W. G., Schulz, C., Lee, T., Jeffries, J. B., and Hanson, R. K., 2003. “Strategies for laser-induced fluorescence detection

of nitric oxide in high-pressure flames. iii. comparison of A – X excitation schemes”. *Appl. Opt.*, **42**(24), pp. 4922–4936.

- [30] DiRosa, M. D., Klavuhn, K. G., and Hanson, R. K., 1996. “LIF spectroscopy of NO and O₂ in high-pressure flames”. *Combust. Sci. Technol.*, **118**(4-6), pp. 257–283.
- [31] Thomsen, D. D., Kuligowski, F. F., and Laurendeau, N. M., 1997. “Background corrections for laser-induced-fluorescence measurements of nitric oxide in lean, high-pressure, premixed methane flames”. *Appl. Opt.*, **36**(15), pp. 3244–3252.
- [32] Bessler, W., and Schulz, C., 2004. “Quantitative multi-line NO-LIF temperature imaging”. *Appl. Phys. B*, **78**(5), pp. 519–533.
- [33] Lee, T., Bessler, W., Kronemayer, H., Schulz, C., and Jeffries, J., 2005. “Quantitative temperature measurements in high-pressure flames with multiline NO-LIF thermometry”. *App. Optics*, **44**(31), pp. 6718–28.
- [34] Bessler, W., Sick, V., and Daily, J., 2003. “A versatile modeling tool for nitric oxide LIF spectra”. *Proc. 3rd Joint Meeting, U.S. Sections of the Combust. Inst.*, **105**, pp. 1–6.
- [35] Luque, J., and Crosley, D., 2013. LIFBASE database and spectral simulation program (version 2.1.1). Tech. rep., SRI International.
- [36] Versailles, P., and Bergthorson, J. M., 2012. “Optimized laminar axisymmetrical nozzle design using a numerically-validated Thwaites method”. *J. Fluids Eng.*, **134**(10).
- [37] Versailles, P., 2017. “CH formation in premixed flames of C₁–C₄ alkanes: assessment of current chemical modelling capability against experiments”. PhD thesis, McGill University.
- [38] Kee, R. J., Miller, J. A., Evans, G. H., and Dixon-Lewis, G., 1989. “A computational model of the structure and extinction of strained, opposed flow, premixed methane-air flames”. *Proc. Combust. Inst.*, **22**(2), pp. 1479–1494.
- [39] Goodwin, D. G., Moffat, H. K., and Speth, R. L., 2016. Cantera: An object-oriented software toolkit for chemical kinetics, thermodynamics, and transport processes. Version 2.3, <http://www.cantera.org>.
- [40] Versailles, P., Watson, G. M. G., Lipardi, A. C. A., and Bergthorson, J. M., 2016. “Quantitative CH measurements in atmospheric-pressure, premixed flames of C₁-C₄ alkanes”. *Combust. Flame*, **165**, pp. 109–124.
- [41] Grcar, J. F., Day, M. S., and Bell, J. B., 2006. “A taxonomy of integral reaction path analysis”. *Combust. Theory Modell.*, **10**(4), pp. 559–579.
- [42] Law, C. K., 2006. *Combustion Physics*. Cambridge University Press.